Journal of Materials Chemistry A

ARTICLE

Electron doping of $Sr_2FeMoO_{6-\delta}$ as high performance anode materials for solid oxide fuel cells

Received 00th October 20xx,
Accepted 00th October 20xx

DOI: 10.1039/x0xx00000x

www.rsc.org/

Xin Yang,[abc] Jing Chen,[d] Dhruba Panthi,[c] Bingbing Niu,[a] Libin Lei,[b] Zhihao Yuan,[e] Yanhai Du,[c] Yongfeng Li,[a] Fanglin Chen,*[b] and Tianmin He*[a]

Electron doping in perovskites is an effective approach to design and tailor the structure and property of materials. In $A_2BB'O_{6-\delta}$-type double perovskites, B-site cation order can be tunable by A-site modification, potentially leading to significant effect on the oxygen nonstoichiometry of the compounds. La^{3+}-doped $Sr_2FeMoO_{6-\delta}$ ($Sr_{2-x}La_xFeMoO_{6-\delta}$, SLFM with $0 \le x \le 1$) double perovskites have been designed and characterized systematically in this study as anode materials for solid oxide fuel cells. Rietveld refinement of powder X-ray diffraction reveals a crystalline symmetry transition of SLFM from tetragonal to orthorhombic with the increase of La content, driven by the extra electron onto the antibonding orbitals of e_g and t_{2g} of Fe/Mo cations. An increase in Fe/Mo anti-site defect accompanies this phase transition. Solid oxide fuel cells incorporating the $Sr_{1.8}La_{0.2}FeMoO_{6-\delta}$ (SLFM2) anode demonstrate impressive power outputs and stable performance under direct CH_4 operation because of its altered electronic structure, desired oxygen vacancy concentration and enhanced reducibility. Density functional theory plus U correction calculations provide an insight into how La doping affects the Fe/Mo anti-site defects and consequently the oxygen transport dynamics.

1. Introduction

Increasing energy demands and environmental concerns have spurred research and development of novel technologies for clean and efficient electricity production. Solid oxide fuel cells (SOFCs) continue to gain interest as one of the most promising power generation technologies because they offer a highly efficient and clean route to convert chemical energy directly to electricity with low pollution.[1] The state-of-the-art nickel–yttrium-stabilized zirconia (Ni–YSZ) anode offers high electrochemical performance but the unavoidable coking readily deactivates Ni, leading to rapid performance degradation under direct hydrocarbon fuel-cell operation.[2–4] Identification of alternative anode materials with coking-resistant properties would play a pivotal role in the advancement of the fuel cell technology.

The use of mixed ionic–electronic conductors (MIECs), especially perovskites, as alternative anode materials addresses the anode deactivation issue. However, most of the perovskite anodes reported to date have anode performance an order of magnitude lower than that of conventional Ni–cermet because of the limited electrical conductivity or insufficient electrochemical activity.[5,6] Oxides of the $A_2BB'O_{6-\delta}$ type are half metallic in nature, where A is rare-earth or alkaline metal (A = Ln, Ca, Sr) and B/B' is transition metal (B = Ni, Fe, Cu, Cr, …; B' = Mo, W, Re, …). The desired conducting property and electrocatalytic activity for the target reactions are tailorable in these oxides. Consequently, double-perovskite anodes have been shown great promise for addressing the problem of coking without decreasing the single-cell performance.[7] Of the available perovskite-structured anodes for SOFCs, the iron-molybdenum systems, such as the B-site ordered $Sr_2FeMoO_{6-\delta}$ (SFM) and redox stable $Sr_2Fe_{1.5}Mo_{0.5}O_{6-\delta}$,[8–10] have generated most attentions owing to their outstanding electrical conductivity, high catalytic activity, thermal stability, and low cost. More recently, $Sr_2FeMo_{0.65}Ni_{0.35}O_{6-\delta}$ has been adopted as the host material to exsolve Ni–Fe alloy nanoparticle catalysts, thus significantly enhancing the catalytic activity of the electrode material.[11]

Metal substitution on either A- or B-site can modify the band filling and oxidation states of the B/B'-site multivalent transition metals. Ca^{2+}/Ba^{2+} substitution for Sr^{2+} has shown improved electrical conductivity in $Ca_2FeMoO_{6-\delta}$, however, the electrochemical activity of $Ca_2FeMoO_{6-\delta}$ and $Ba_2FeMoO_{6-\delta}$ have been observed to decrease.[12] Electron doping in $Sr_2FeMoO_{6-\delta}$ via partial substitution of heterovalent lanthanide elements for Sr^{2+} is another approach to modify its conductivity and electrochemical activity for fuel oxidation.[13] Notably, the distribution of Fe and Mo in $Sr_2FeMoO_{6-\delta}$ is not fully ordered because of the similar ionic radii of Fe^{3+} (0.645 Å) and Mo^{6+} (0.61 Å) in the six-fold coordination, i.e., the presence of anti-site defects (ADs) in the two interleaving sublattices is significant

[a] Key Laboratory of Physics and Technology for Advanced Batteries, Ministry of Education, College of Physics, Jilin University, Changchun 130012, PR China.
[b] Department of Mechanical Engineering, University of South Carolina, 300 Main Street, Columbia, SC 29208, USA.
[c] College of Aeronautics and Engineering, Kent State University, 1400 Lefton Esplanade, Kent, OH 44242, USA.
[d] School of Chemistry and Chemical Engineering, Henan University of Technology, Zhengzhou 450001, PR China.
[e] School of Materials Science and Engineering, Tianjin University of Technology, Tianjin 300384, PR China.

Electronic Supplementary Information (ESI) available: [details of any supplementary information available should be included here]. See DOI: 10.1039/x0xx00000x

(~ 8%).[14] The ADs alter the Fe–O–Mo bonding network and the electron-hopping pathway, making its half metallic character quite sensitive to and consequently tunable via the degree of ADs.[15] Recently, it has been reported that the La^{3+}/Gd^{3+} substitution for Sr^{2+} increases the AD concentration as well as the density of electrons at the Fermi level.[16,17] In this respect, it will be of great interest to investigate the possible modification in crystalline structure, electrical conductivity, oxygen nonstoichiometry, and electrochemical activity for fuel oxidation induced by electron doping, especially under the SOFC operation.

In the present work, the effects of A-site La-doping on the crystalline structure, electronic properties, and electrode performance in SOFCs with double-perovskite $Sr_{2-x}La_xFeMoO_{6-\delta}$ (SLFM, $0 \le x \le 1$) anodes have been investigated. The experimental results show that $Sr_{1.8}La_{0.2}FeMoO_{6-\delta}$ (x = 0.2, SLFM2) anode has significantly improved electrical conductivity and electrochemical activity, especially when operating in CH_4. In contrast, excess La doping seems to suppress the electrode performance, accompanied by a decrease in structural symmetry. First principles calculations are used to further understand the electrical and electrochemical properties transformation. The methane conversion over the SLFM catalysts suggests that the high methane conversion is likely to account for the attractive electrochemical performance of SLFM2 in methane.

2. Experimental section

2.1 Material synthesis

$Sr_{2-x}La_xFeMoO_{6-\delta}$ (x = 0, 0.2, 0.4, 0.6, 0.8, 1.0) were synthesized *via* a solid-state route. Stoichiometric amounts of La_2O_3, $SrCO_3$, Fe_2O_3, and MoO_3 were ball-milled with ethanol and deionized water for 12 h. The dried powders were pelletized and pre-fired in air for 10 h at 900 °C. The calcined pellets were crushed and ball-milled for another 12 h, then pelletized and sintered in air for 10 h at 1000 °C to form submicron powders. This process was repeated, followed by final calcination in 5% H_2/95% N_2 at 1200 °C for 12 h to achieve single phases. After the XRD phase purity identification, the as-prepared pellets were ground to powders and pressed into rectangular bars ($40 \times 6 \times 2$ mm^3) and then sintered in 5% H_2/95% N_2 for 5 h at 1300 °C to achieve a dense structure for electrical conductivity measurements. $Y_{0.92}Zr_{0.08}O_{2-\delta}$ (YSZ), $Ce_{0.9}Ge_{0.1}O_{2-\delta}$ (GDC) and $La_{0.9}Sr_{0.1}Ga_{0.8}Mg_{0.2}O_{3-\delta}$ (LSGM, all from Fuel Cell Materials) electrolyte powders were pressed into pellets and sintered for 5 h at 1400 °C (YSZ) and 1450 °C (GDC and LSGM), respectively. Dense YSZ support was obtained by polishing the white YSZ disk (12.14 mm in diameter) with a pneumatic grinder to 300 μm thick. LSCF cathode ink (Fuel Cell Materials) was applied directly for cell fabrication.

2.2 Assembly of cell configuration

The button-type YSZ electrolyte-supported SOFC with configuration SLFM/GDC/300 μm-YSZ/GDC/$La_{0.6}Sr_{0.2}Co_{0.8}Fe_{0.2}O_{3-\delta}$ (LSCF) were constructed for single-cell performance measurement. Symmetrical cells with configuration SLFM/GDC/300 μm-YSZ/GDC/SLFM were fabricated for electrochemical impedance spectroscopy (EIS) testing. Ni–YSZ-anode cells with identical configuration were fabricated for comparison. The GDC and anode inks were made by mixing and grinding proper amounts of polyvinyl butyral (B-98, Sigma Aldrich, USA) and ceramic powders for 1 h. The GDC ink was screen-printed on both sides of the YSZ support and then sintered at 1400 °C for 5 h as a buffer layer. The SLFM anode ink was screen-printed over the GDC buffer layer of the supporting disk and then sintered in 5% H_2/95% N_2 for 3 h at 1100 °C. The LSCF cathode ink was screen-printed on the other side of the YSZ support, followed by sintering in 5% H_2/95%N_2 for 3 h at 900 °C. The active area of the electrodes was 0.385 cm^2. Platinum paste (CL11-5349, Heraeus electronics, USA) was brushed onto the electrodes as the current collector. An alumina tube was used as the fuel cell holder and the anode compartment. Silver conductor paste (C8728, Heraeus, USA) was applied for the connection of silver wires and the platinum current collector. High-temperature seal (Ceramabond, 552-11-5, Aremco, USA) was used to seal the cell to an alumina tube.

2.3 Structural characterization

The phase purity of SLFM was identified by X-ray diffractometer (XRD, Rigaku D/Max-2100, Cu Kα radiation, λ = 1.5418 Å) on well-calcined powders over a scanning range of 20–120° in a step of 0.015° and at a scanning rate of 1° min^{-1}, and analyzed by Fullprof Rietveld refinement. SAED and HRTEM observations were performed on JEM-2100F (136 eV).

2.4 Electrical conductivity measurement

The electrical conductivity of the SLFM series was measured in hydrogen in a 300–800 °C range with a four-probe configuration using a Solartron SI 1287 Electrochemical Interface combined with SI 1260 Impedance/Gain–Phase Analyzer. Ag wire and Pt paste were used as the four probes and the conductors, respectively. An alumina tube with at least 5 isolated channels was used as the sample holder providing the testing atmosphere and separating the wires. The bar-shaped dense sample was reduced in pure hydrogen for 2 h at 800 °C before the measurements to ensure the complete reduction of anode. The dynamic electric current was set to a range of −0.5–0.5 A, and then the voltage was recorded, where the slope equals to the DC resistance.

2.5 Material surface analysis

The X-ray photoelectron spectra (XPS) were acquired on a photoelectron spectrometer (Kratos Axis Ultra DLD) equipped with a monochromated AlKα (1486.6 eV) X-ray source and hemispherical analyzer. The O 1*s*, C *1s*, Mo 3*d*, and Fe 2*p* core-level high-resolution spectra of the SLFM powders were recorded under 225 W with a pass energy of 160 eV. The peak profile was deconvoluted using a standard XPSPEAK software to resolve the separate constituents after background subtraction. The C 1*s* calibration to 284.6 eV was made before analysis. The morphology of the SLFM anodes were analyzed using a field emission scanning electron microscope (FESEM, Sirion 200, FEI, USA) at 15–20 kV attached with energy dispersive X-ray spectroscopy (EDS, Oxford).

2.6 Thermal gravimetric analysis

The temperature dependence of oxygen nonstoichiometry ($6-\delta$) of the SLFM powders was determined by thermal gravimetric analysis (TGA, SDT Q600, TA Instruments, USA). All powders (20 mg) were pretreated in air for 2 h at 150 °C to eliminate the surface adsorbed molecular water prior to the TGA measurement. N_2 was

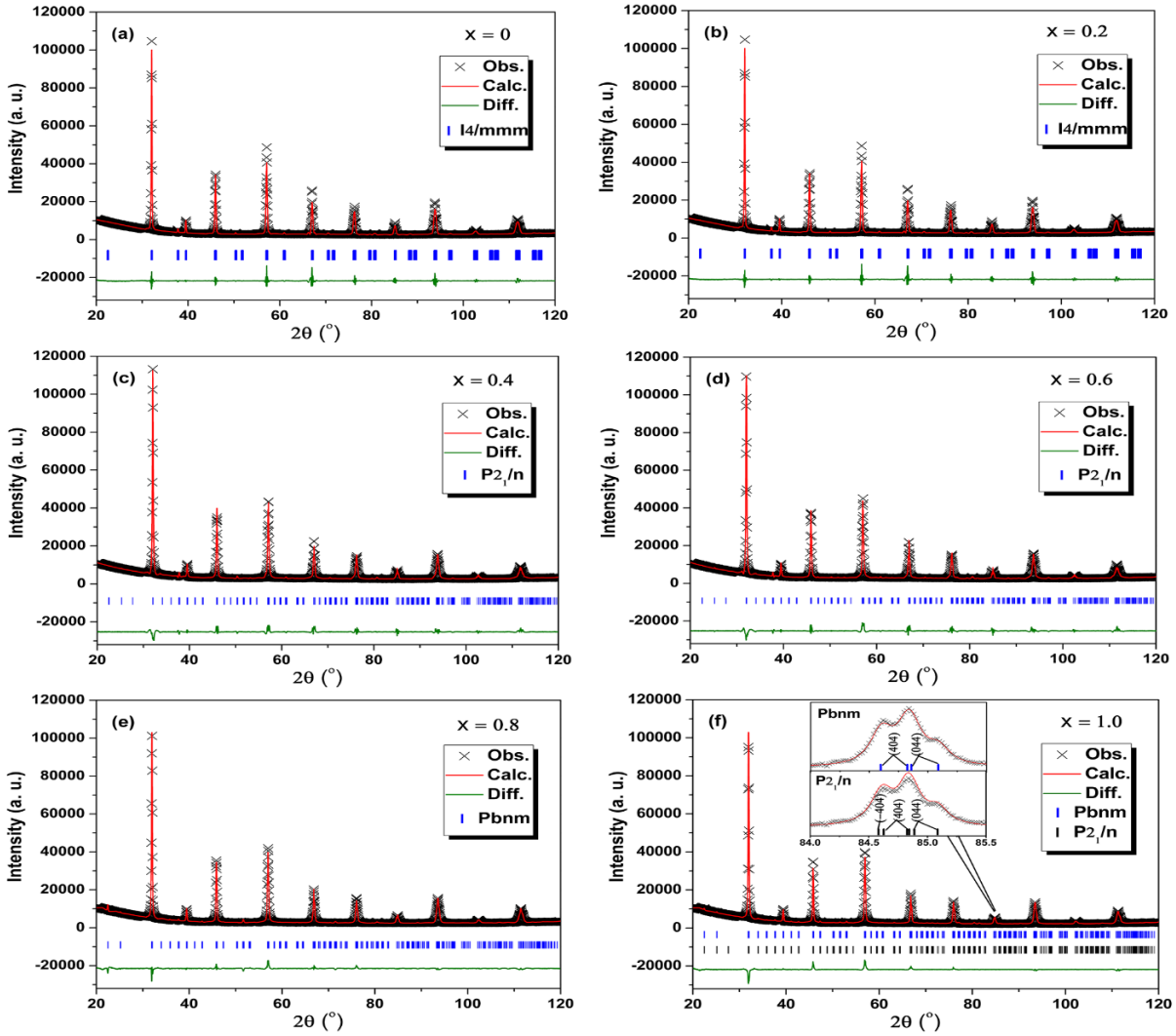

Fig. 1 Rietveld refinement profiles of $Sr_{2-x}La_xFeMoO_{6-\delta}$ to powder XRD collected at room temperature: (a) x = 0 (*I 4/mmm*); (b) x = 0.2 (*I 4/mmm*); (c) x = 0.4 (*P* $2_1/n$); (d) x = 0.6 (*P* $2_1/n$); (e) x = 0.8 (*P bnm*); and (f) x = 1.0 (*P bnm*). The inset in (f) shows the refinement profiles in comparison with *P* $2_1/n$.

flowed at 100 mL min^{-1} for 2 h at RT to remove air from the instrument, followed by heating up to 900 °C at 10 ° min^{-1}.

2.7 Reducibility and methane conversion capability characterization

The temperature-programmed reduction (H_2-TPR) was carried out using a dynamic chemisorption analyzer (PCA-1200, Builder, China) to investigate the reducibility of the SLFM powders. After pretreated for 10 min in N_2 at 300 °C, zero adjustment was conducted by flowing 5% H_2/95% Ar at a rate of 30 mL min^{-1} prior to the measurement. The H_2 consumption was recorded in a temperature range of 30–1000 °C at a heating rate of 10 °C min^{-1}.

The methane conversion capability of the SLFM catalysts was determined using a fixed-bed reactor and a gas chromatograph (GC-7820 A, Agilent, USA). 2.0 g of sample was loaded into the quartz tube to react with the reagent gas. N_2 was fed at a flow rate of 50 mL min^{-1} for 1 h to remove air. Then the feed gas was switched to a mixture of reactant gas and shielding gas (40% CH_4 + 60% N_2). The methane conversion was recorded from 300 °C to 1000 °C increasing in steps of 25 °C min^{-1} after 10 min on-stream operation to reach the steady state. The CH_4 conversion rate and syngas selectivity were calculated as described elsewhere. [18]

2.8 Fuel cell testing

The EIS and the current density–voltage curves were performed on a multi-channel electrochemical testing system (Versa STAT, Princeton Applied Research, USA). The EIS was recorded under open-circuit voltage (OCV) over a frequency range of 0.1–10^5 Hz. Slightly humidified hydrogen and methane (3% H_2O) were used as the feed gases with ambient air as the oxidant, respectively. The flow rate was controlled at 40 sccm by a mass flow controller (APEX, Alicat Scientific). The coking tolerance was evaluated under a constant current of 0.3 A cm^{-2} at 800 °C for a 45 h of operation.

2.9 Computational information

First-principles calculations based on the density functional theory (DFT) were performed using the VASP code. The band structure, $E_{form}AD$ and $E_{form}O^*$ were estimated based on the GGA + U.

The magnetic arrangement of Fe and Mo was controlled to antiferromagnetical (AF) alignment with Fe in a high spin configuration to achieve the most stable state, according to previous experimental observations and GGA+U (and LDA+U) calculations on this system.[15, 19] The parameter value of $(U–J)_{Fe}$ = 4.0 eV for the strongly localized 3*d* electrons of Fe was applied. A $\sqrt{2} \times \sqrt{2} \times 1$ 40-atom $Sr_7LaFe_4Mo_4O_{24}$ (x = 0.2) pseudocubic supercell, which contains approximately 4 SLFM2 formula units (tetragonal), was used as the initial model for calculations, as shown in Supplementary Fig. S10. All calculations were computed after full geometry optimization. The (partial) density of the states, $E_{form}AD$ and $E_{form}O^*$ ($E_{formO}^* = E_{defect} - E_{host} + 1/2E_{O2}$ (g)) were computed based on the perfect structures and structures with ADs or/and oxygen vacancies with respect to the experimental results.[15]

3. Results and discussion

3.1 Structural and physical property characterization of $Sr_{2-x}La_xFeMoO_{6-\delta}$ compounds

The XRD patterns characterized on SLFM powders are shown in Fig. S1 (Supporting Information). The SLFM series was perfectly phase pure with no traces of previously reported $SrMoO_4$ impurity observed, indicating the complete reduction.[20] The increased La content resulted in a shift of the XRD peaks to lower Bragg angles, corresponding to a cell expansion,[21,22] although the cation size of La^{3+} (1.36 Å) is smaller than that of Sr^{2+} (1.44 Å). This is because the electronic effect of La^{3+} is dominant, instead of the ionic size. Detailed quantitative Rietveld analysis of the XRD patterns with structural information are shown in Fig. 1 and Table 1. The SFM crystalized in the tetragonal (*I 4/mmm*) space group. Structural transitions from tetragonal to monoclinic (*P 2₁ /n*) and to orthorhombic (*P bnm*) distortion were found with La doping at $x \geq 0.4$ and $x \geq 0.8$, respectively. For all SLFM compositions, well refinement could not be obtained without taking the Fe/Mo cationic disorder into account, i.e., the presence of AD had to be considered. Similar trend has been reported in the Gd^{3+}/Nd^{3+} substituted SFM counterparts.[7,17] The AD concentration is defined as the ratio occupancy of B-cation at the B'-site. Although the tetragonal symmetry was maintained for the SLFM2, the cation order ($\eta = 1 - 2 \times$ AD) was found to decrease dramatically from 84.31 % (x = 0) to 34.92 % (x = 0.2). The order degree continued to decrease with increased La content. For the compositions with $0.8 \leq x \leq 1.0$, successful refinements were achieved with either *P 2₁/n* or *P bnm* space group, where the latter gave a better goodness of refinement. The inset in Fig. 1(f) shows an expanded view of the refinement results for the x = 1.0 compound in both cases. It is noteworthy that an AD = 50 % or η = 0 corresponds to a totally disordered double perovskite. Therefore, the $0.8 \leq x \leq 1.0$ compounds with extremely low order degree were nearly B-site disordered. We indexed the $0.8 \leq x \leq 1.0$ compounds to the orthorhombic (*P bnm*) structure according to their highly-disordered nature and the electrochemical behavior as described afterwards.

Table 1 Main crystallographic information for $Sr_{2-x}La_xFeMoO_{6-\delta}$ derived from Rietveld refinement of the XRD

	Space group	*I 4/mmm*		*P 2₁/n*		*P bnm*	
	Sample	**x = 0**	**x = 0.2**	**x = 0.4**	**x = 0.6**	**x = 0.8**	**x = 1.0**
Unite-cell parameters	a (Å)	5.5751(0)	5.5801(0)	5.5834(2)	5.5899(0)	5.5899(1)	5.6121(2)
	b (Å)	5.5751(0)	5.5801(0)	5.5787(3)	5.5846(6)	5.6110(1)	5.5939(4)
	c (Å)	7.9048(0)	7.9116(6)	7.9100(9)	7.9169(7)	7.9067(2)	7.9140(7)
	V (Å^3)	245.69(0)	246.34(9)	246.37(4)	247.13(8)	247.99(1)	248.45(3)
	β (°)	90	90	89.8251(9)	89.8271(4)	90	90
Fe Occupancy[a]	Normal site	0.9215(4)	0.674(6)	0.6532(5)	0.6301(2)	0.5799(9)	0.5477(7)
	Disordered	0.0784(6)	0.325(4)	0.3467(5)	0.3698(8)	0.4200(1)	0.4522(2)
Order	η (%)	84.31	34.92	30.65	26.02	15.99	9.56
Averaged Bond length[b]	$d_{Sr/La-O}$ (Å)	2.8042(2)	2.7935(1)	2.6774(0)	2.6773(3)	2.6682(1)	2.6631(2)
	d_{Fe-O} (Å)	2.0067(6)	2.0054(6)	2.0009(1)	1.9910(6)	1.9998(6)	2.0005(6)
	d_{Mo-O} (Å)	1.9422(3)	1.9592(6)	1.9718(4)	1.9897(6)	1.9998(2)	2.0021(9)
Bond angle[c]	$\alpha_{Fe-O1-Mo}$ (°)	180	180	165.8420	165.407	161.907	159.910
	$\alpha_{Fe-O2-Mo}$ (°)	180	180	164.779	163.222	162.628	161.878
Reliability factors	χ^2	1.8	4.2	3.8	2.0	2.4	3.5
	R_p (%)	2.17	2.31	3.24	3.67	2.98	3.05
	R_{wp} (%)	1.36	2.02	2.12	1.61	4.39	4.45

[a)]Refinement of Mo and Fe occupancies showed slight deviation, indicating the presence of some cation vacancies; [b)]Calculated average value of bond lengths of major metal—oxygen atoms are given; [c)]Oxygen atoms labeled as O1 and O2 denote the O positions along the *c* axis, and in the *ab* plane, respectively. For $0.4 \leq x \leq 1.0$, the oxygen atoms are slightly off the *c* axis or the *ab* plane because of octahedral distortion.

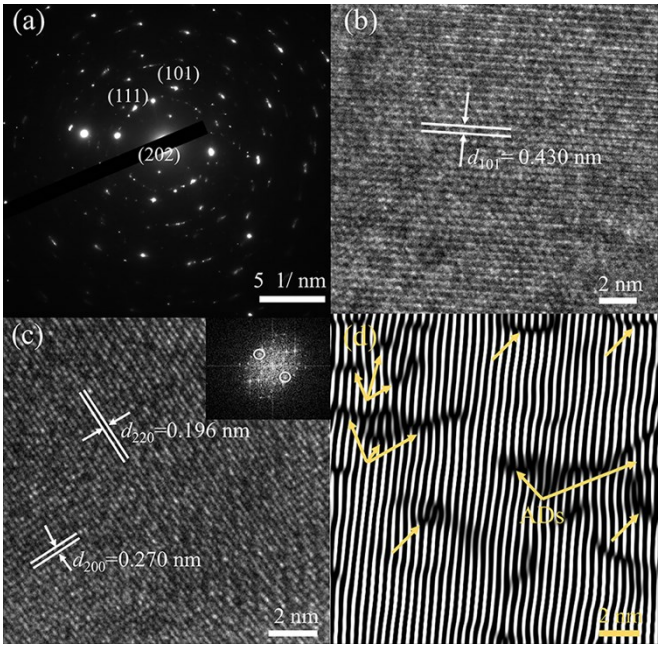

Fig. 3 (a) SAED patterns of the $Sr_{1.8}La_{0.2}FeMoO_{6-\delta}$ catalyst; (b, c) HRTEM image of the $Sr_{1.8}La_{0.2}FeMoO_{6-\delta}$ catalyst. Inset is the corresponding FFT image; (d) Inverse FFT image of (c) with many anti-site defects marked with arrows.

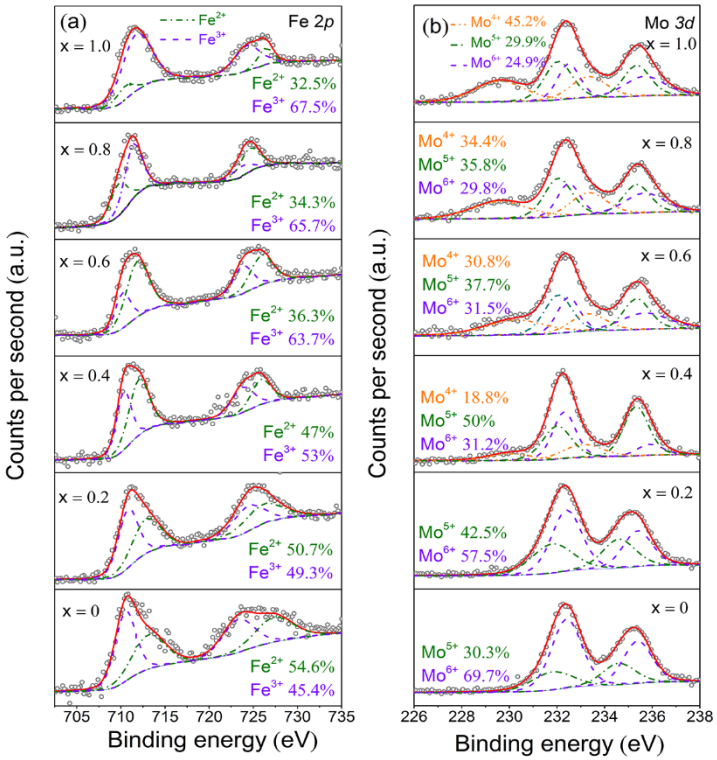

Fig. 2 XPS peak fitting results of $Sr_{2-x}La_xFeMoO_{6-\delta}$($0 \le x \le 1$): (a) Fe *2p* and (b) Mo *3d*

As shown in **Table 1**, the bond angles of Fe–O–Mo along the *c* axis and in the *ab* plane continued to decrease as the doping level increased, corresponding to the reduction of symmetry. After La doping, the averaged bond length of Sr/La–O decreased whereas the averaged bond length of Mo–O increased. It is likely that Sr/La moved toward O to support more electrons to form Sr/La–O bond; Mo moved away from O to give less electrons to form Mo–O bond. The Fe–O bond remained nearly unchanged in length. Thus, we may assume that the electron doping has little effect on the valence state of Fe, while the valence state of Mo decreases significantly to receive the electron, i.e., the electron is mainly injected into the Mo orbit by La doping. As the ionic radius of Mo^{5+} (Mo^{4+}) is larger than that of Mo^{6+}, the increase in cell volume results from the change in the valence states of Mo ions caused by the electronic effect.

The crystal structure of the SLFM2 was further confirmed by the selected-area electron diffraction (SAED). Fig. 2(a) shows the SAED pattern of the SLFM2 powder, which can be indexed to the tetragonal group [23]. The presence of the (101) plane indicates a mainly ordered double-perovskite structure of the SLFM2. The defect nature in the mainly ordered structure was revealed by the high-resolution transmission electron microscopy (HRTEM). Fig. 2(b) shows the HRTEM image with the d-spacing of the (101) plane, the intensity of which is strongly related to the AD concentration. The (101) plane in a tetragonal unit cell corresponds to the (111) superstructure reflections of the pseudocubic supercell, as confirmed in the XRD patterns reported previously.[20] As shown in Fig. 2(c), the HRTEM clearly displays alternative dark-bright strips, corresponding to the alternation of the Fe/Mo sites, which are consistent with the HRTEM observations of layered double-perovskites.[24] Fig. 2(d) shows the corresponding inverse Fast Fourier Transform (FFT) image of Fig. 2(c). The presence of many ADs becomes clear in the inverse FFT image, which is in accord with our XRD refinement results.

To identify the evolution of Fe and Mo oxidation states and to estimate the oxygen vacancy concentration, XPS spectra were recorded at room temperature. As depicted in Supplementary Fig. S2, under the combination of La doping on the Sr-site and cation-disorder contribution, slightly La-doped sample (x = 0.2) exhibited a high adsorbed oxygen species (O_{ad}) percentage in the SLFM series at room temperature, which would be readily released to form oxygen vacancies so as to faciliate the suface reaction of the anode in a SOFC.[25] Similar evolution of the O_{ad} percentage with A-site Ce doping has been reported in the literature.[26] Fig. 3 shows the Fe *2p* and Mo *3d* core-level spectra. Fe was observed to present in a mixed oxidation state of $Fe^{2+/3+}$ for all samples. The calculated valence of Fe increased slightly from $Fe^{2.45+}$ to $Fe^{2.67+}$ with increasing x, indicating the little effect by heterovelant doping. In contrast, the valence of Mo showed remarkable change upon La doping. For the $0 \le x \le 0.2$ compositions, Mo existed in a mixed oxidation state of $Mo^{5+/6+}$, whereas heavy La doping led to the appearance of Mo^{4+} ($Mo^{4+/5+/6+}$). The calculated valence of Mo decreased from $Mo^{5.7+}$ to $Mo^{4.8+}$ with increasing La content, which is consistent with the previous reports based on the Mössbauer spectra.[27] This strongly suggests that most of the itinerant electrons introduced by La substitution for Sr ($La_{Sr}^{\cdot}$) were received by the neighboring Mo ions ($Mo_{Mo}^{\times}$), thus decreasing the valence state of Mo to maintain the electro-neutrality.[21] The defect equations can be written as follows: ($La_{Sr}^{\cdot}$) were received by the neighboring Mo ions ($Mo_{Mo}^{\times}$), thus

$$La_2O_3 \xrightarrow{SrO} 2La_{Sr}^{\cdot} + 2e' + 2O_O^{\times} + 1/2\,O_2 \uparrow, \quad (1)$$

$$Mo_{Mo}^{\times} + e' \rightarrow Mo_{Mo}'. \quad (2)$$

The calculated difference of Fe/Mo valences decreases from 3.25 to 2.13, which is believed to be the origin of the AD formation.[28] Consequently, low-valent Mo ions (presumably $Mo^{4+/5+}$) would prefer to locate at the anti-sites while the high-valent $Mo^{5+/6+}$ would remain at the right sites as the La content increases. Therefore, the large AD concentration can be considered as a manifestation of the increased low-valent $Mo^{4+/5+}$ concentration upon La doping.

To evaluate the reducibility of the prepared catalysts，one of the key performance metrics，H_2-TPR was performed as shown in Fig. 4(a). A small low-temperature reduction peak (400–700 °C) and a large high-temperature reduction peak (700–1000 °C) were present for all the samples. For pure SFM, the low-temperature peaks appeared at 545 °C and 661.4 °C, corresponding to the reduction of the superficial adsorbed oxygen species (O_{ad}+ $H_2 \rightarrow H_2O$) and $Mo^{6+} \rightarrow Mo^{5+}/Mo^{4+}$ reduction, respectively.[29] The high-temperature peak appeared at 913.5 °C, which can be attributed to the reduction of bulk lattice oxygen and simultaneously $Fe^{3+} \rightarrow Fe^{2+}$.[30] For SLFM2, the reducibility was significantly improved via lowering the reduction temperature and increasing the amount of hydrogen consumption, which indicates more active oxygen species were available for fuel oxidation in the SLFM2 catalyst. Under this assumption, the $0.4 \leq x \leq 1$ compositions showed decreased reducibility. The high-temperature reduction peaks appeared beyond 1000 °C in heavily La-doped samples ($0.8 \leq x \leq 1.0$), which was similar to that of single-perovskite $LaFeO_{3-\delta}$, indicating the smaller Fe/Mo valence difference.[31]

To evaluate the thermal stabilities of SLFM samples, thermogravimetric analysis (TGA) was carried out in N_2 within the 30–900 °C temperature range, as shown in Fig. 4(b). Three weight-loss regions were present in the TGA plots for all samples. The initial weight loss may be related to the removal of adsorbed species (H_2O, CO_2) after synthesis below 200 °C. According to our H_2-TPR analysis, the accelerated weight loss within the 200–800 °C temperature range is associated with the break of Mo–O, generating oxygen vacancies ($V_O^{\cdot\cdot}$), i.e., the reduction of Mo^{6+} to Mo^{5+} and even Mo^{4+} corresponds to the predominant defect equation (3) and (4):

$$2Mo_{Mo}^{\times} + O_O^{\times} \leftrightarrow 2Mo_{Mo}' + V_O^{\cdot\cdot} + 1/2\, O_2 \uparrow, \quad (3)$$

$$2Mo_{Mo}^{\cdot} + O_O^{\times} \leftrightarrow 2Mo_{Mo}'' + V_O^{\cdot\cdot} + 1/2\, O_2 \uparrow. \quad (4)$$

The accelerated weight loss at ≥ 750 °C, especially for SLFM2, is associated with the reduction of Fe^{3+} ($Fe_{Fe}^{\times}$) to Fe^{2+} (Fe_{Fe}') *via*

$$2Fe_{Fe}^{\times} + O_O^{\times} \leftrightarrow 2Fe_{Fe}' + V_O^{\cdot\cdot} + 1/2\, O_2 \uparrow, \quad (5)$$

releasing plenty of oxygen vacancies.

Chemically, electron doping on the A-site of double-perovskite oxides generally leads to a decrease in oxygen vacancies to compensate the extra charge introduced. Interestingly, as depicted in the TGA plots, the SLFM2 exhibited higher oxygen loss at elevated temperatures among the SLFM series. This might be because the presence of a certain amount of ADs in the SLFM2 can modify the oxygen nonstoichiometry within a low electron-doping concentration. Therefore, the TGA combined with H_2-TPR results hint at an improved anodic performance of the SLFM2.

The temperature dependence of the electrical conductivity, σ, for

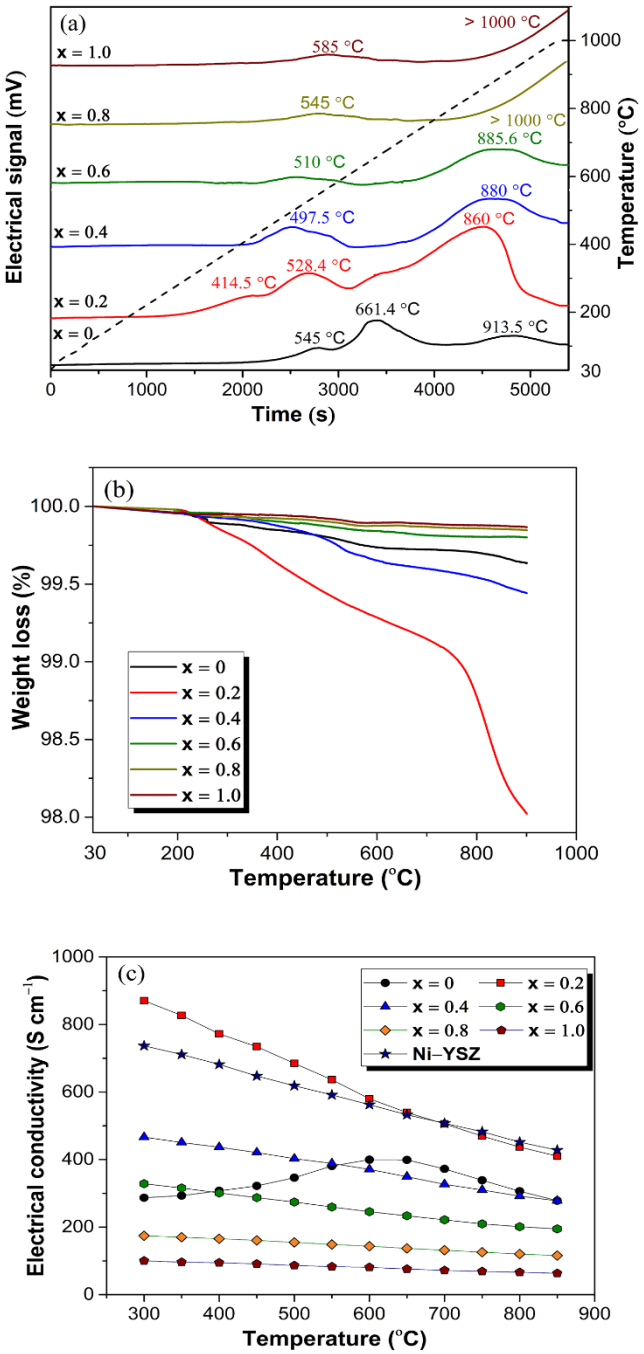

Fig. 4 (a) H_2-TPR plots of $Sr_{2-x}La_xFeMoO_{6-\delta}$ ($0 \leq x \leq 1$) catalysts; (b) TGA profiles of $Sr_{2-x}La_xFeMoO_{6-\delta}$ measured in N_2; (c) Electrical conductivity of $Sr_{2-x}La_xFeMoO_{6-\delta}$ and Ni–YSZ in H_2.

SLFM in comparison with Ni–YSZ in H_2 is shown in Fig. 4(c). As expected, improved electrical conductivity was observed in SLFM2, which is comparable to that of Ni–YSZ. The electrical conductivity of SLFM ranged from 85 to 460 S cm^{-1} in H_2 at 800 °C, which is an order of magnitude higher than the typical perovskite anode materials previously reported, such as $Sr_2MMoO_{6-\delta}$ (M = Mg, Mn, Ni, Co, σ = 1.1–8.6 S cm^{-1}),[32,33] $Sr_{1.4}La_{0.6}MgMoO_{6-\delta}$ (7.5 S cm^{-1}),[34] and $Pr_2BaMnO_{5+\delta}$(8.6 S cm^{-1} in 5% H_2).[24]

However, the electrical conductivity starts to decrease when $x \geq 0.4$, accompanied by the reduction of symmetry and the degree of cation ordering. This is because heavy Fe/Mo disorder may suppress

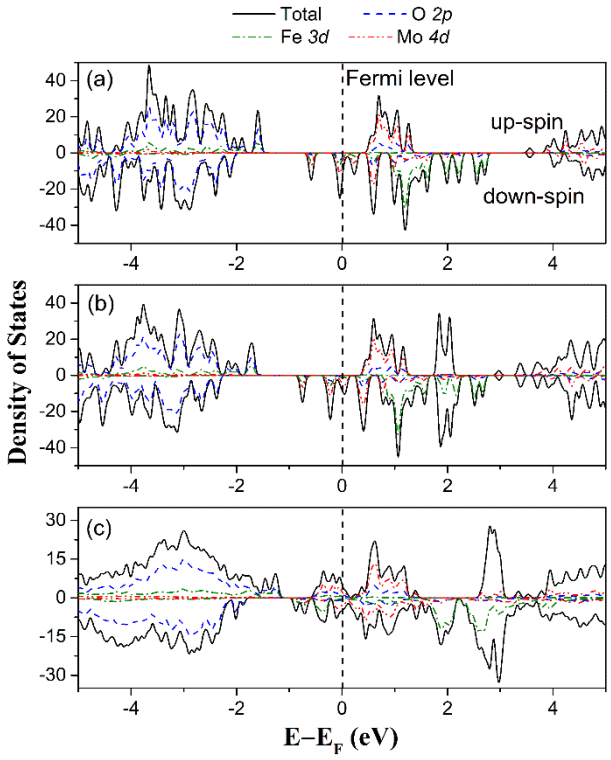

Fig. 5 Total and partial density of states of (a) perfect $Sr_8Fe_4Mo_4O_{24}$; (b) perfect $Sr_7LaFe_4Mo_4O_{24}$; (c) $Sr_7LaFe_4Mo_4O_{23}$ with 25% AD in the *ab* plane and a O^* along the Fe–O^*–Fe_{Mo}.

the double-exchange interaction between the Fe_B–O–Mo_B–O–Fe_B.[17,20] Moreover, the increased d_{Mo-O} distance and decreased $\alpha_{Fe-O-Mo}$ angle observed in our XRD refinement can also disturb the double-exchange interaction.[35] Supplementary Fig. S3 and S4 show the SEM morphology and BET surface area of the SLFM powders, respectively. Apparently, the average grain size was effectively decreased by La doping. The specific BET area also showed monotonic increase with increasing La content. Consequently, the extrinsic grain-boundary contributions to the electrical conductivity can be excluded.

As depicted in Fig. 4(c), pure SFM parent exhibited a transition from semiconducting to metal-like conducting behavior, whereas all La-substituted samples only exhibited a metal-like conducting behavior. The conducting mechanism in SFM and SLFM seems to be different. To unveil the doping effect on the band structure, DFT calculations were performed. The spin-polarized generalized gradient approximation (GGA) +U Hubbard contribution calculations regarding the band structure for SFM and SLFM2 (with and without ADs) can provide a deeper insight into the effect of La doping and ADs on the conducting mechanism. On the basis of our XRD refinement results, a $\sqrt{2} \times \sqrt{2} \times 1$ pseudocubic supercell $Sr_7LaFe_4Mo_4O_{24}$ ($Sr_8Fe_4Mo_4O_{24}$) was created as the initial model for calculations (see Supplementary Fig. S5). In Fig. 5(a), the band structure of the perfect SFM presents a half-metal character with the down-spin conduction band crossing the Fermi level (E_F). The down-spin channel near E_F is formed mostly by the Mo ($4d_{t_{2g}}\downarrow$), where the Fe ($3d_{t_{2g}}\downarrow$) and O (*2p*) sub-bands have also made important contributions. This is because the Mo ($4d_{t_{2g}}\downarrow$), Fe ($3d_{t_{2g}}\downarrow$)and O (*2p*) states are strongly hybridized, responsible for the electron hopping.[15] Replacing a Sr^{2+} ion by a La^{3+} in perfectly ordered $Sr_8Fe_4Mo_4O_{24}$ introduces one electron into the matrix. As the electron only contributes to the minority spin band, the half-metal character is still maintained, as shown in Fig. 5(b). The bandgap between the Fe e_g and Mo t_{2g} around the E_F is increased from 1.89 to 1.92 eV, corresponding to a limited improvement in half metallic feature. However, a large amount of ADs has been observed experimentally in the SLFM oxides. Therefore, the calculations based on the perfect SLFM2 structure do not reflect the actual density of states. The presence of ADs should be taken into account. In addition, an oxygen vacancy (O^*) was created to give a true picture of the electronic structure. Fig. 5(c) shows the total and various partial density of states (DOS) for the La-doped structure with 25 % ADs (for example, in the *ab* plane) and an O^* (along the Fe–O^*–Fe_{Mo}), which has been proved to be the most probable structure according to the principle of minimum energy. As depicted in Fig. 5(c), the Fe e_g–Mo t_{2g} gap around the E_F observed in the ordered DOS is filled. As both the up- and down-spin channels cross the E_F, the spin-polarized half-metal character no longer exists, i.e., the SLFM2 exhibits a metal-like feature. The most evident effect of the presence of cation disorder is the destruction of the half-metal feature. Consequently, La incorporation into the Sr-sublattice accompanied by a drastic increase in AD concentration affects the electrical conductivity of SLFM via a conduction-mechanism transition from semiconducting to metallic-like conducting. The GGA+U prediction above is also in qualitative agreement with our experimental results as depicted in Fig. 4(c).

3.2 Electrochemical performance of $Sr_{2-x}La_xFeMoO_{6-\delta}$ anodes

The electrochemical performance of the SLFM anodes was characterized by electrochemical impedance spectroscopy (EIS) using YSZ electrolyte-supported symmetrical cells. Symmetrical cells were fabricated based on the chemical compatibility and thermal expansion coefficient match between the SLFM anode and the commonly used electrolytes to achieve high cell performance and long-term stability (see Supplementary Fig. S6 and S7). The chemical compatibility results based on the SLFM2 anode suggest that LSFM may be susceptible to react with LSGM electrolyte at 1100 °C to form insulating $SrLaGa_3O_7$ phase. Since YSZ is the most-widely used electrolyte material, it is chosen as the electrolyte to evaluate SLFM anode performance. GDC buffer layer was included between the SLFM anode and YSZ electrolyte since SLFM can potentially react with YSZ, forming $SrMoO_4$, $SrZrO_3$ and other insulating impurities. Consequently, GDC/YSZ/GDC electrolyte structure is adopted in this study for the symmetrical cell evaluation of the SLFM anode. Fig. 6(a) shows the normalized SLFM anode electrochemical impedance spectra measured under OCV in H_2 at 800 °C. The area specific resistance (ASR) values are 0.48, 0.35, 0.41, 0.63, 0.79 and 0.83 $\Omega \cdot cm^2$ for x = 0, 0.2, 0.4, 0.6, 0.8 and 1, respectively. The SLFM2 anode possesses the lowest area specific resistance among the SLFM series, while the area specific resistance continues to increase once the La content is increased beyond x = 0.2. The Arrhenius plots of ASR for hydrogen oxidation reaction (HOR), as determined from the EIS data, is plotted in Fig. 6(b). The activation energies calculated from the slopes of ASR curves are 0.73 eV for SFM and 0.59 eV for SLFM2 anode, respectively, indicating that the improvement in catalytic activity with La-doping in SFM is achieved. Excess La addition would lead to a decrease in the electrochemical activity of the SLFM anodes.

Journal of Materials Chemistry A

ARTICLE

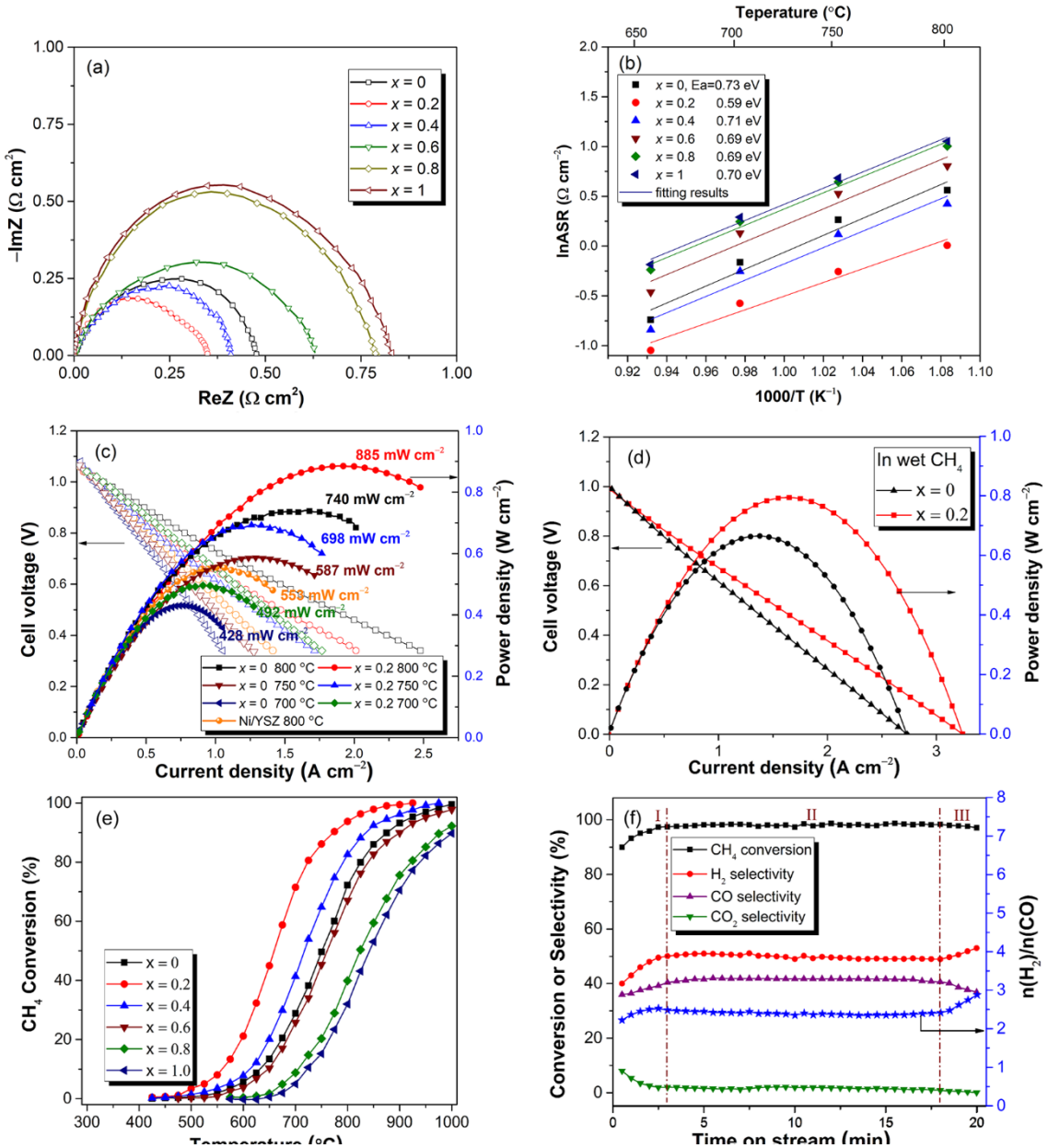

Fig. 6 Impedance spectra of $Sr_{2-x}La_xFeMoO_{6-\delta}$ ($0 \le x \le 1$) electrode on GDC/YSZ/GDC electrolyte under OCV: (a) measured at 800 °C, normalized Nyquist plots, and (b) from 650 to 800 °C, Arrhenius plots; Typical current-voltage characteristics and corresponding power densities of single cell $Sr_{2-x}La_xFeMoO_{6-\delta}$/GDC/300 μm-YSZ/GDC/LSCF: (c) in wet H_2 for $0 \le x \le 0.2$ in comparison with Ni–YSZ from 700 to 800 °C, and (d) in wet CH_4 for $0 \le x \le 0.2$ at 800 °C; (e)Temperature dependence of methane conversion over the $Sr_{2-x}La_xFeMoO_{6-\delta}$($0 \le x \le 1$) catalysts; (f) Catalytic performance of $Sr_{1.8}La_{0.2}FeMoO_{6-\delta}$ for methane selective oxidation.

Consequently, the SLFM2 composition was adopted as the anode for fuel cell fabrications to achieve improved power output.

The electrochemical performance of single cells with the configuration of SLFM2/GDC/300 μm-YSZ/GDC/LSCF in slightly humidified H_2 and CH_4 (3% H_2O) at different temperature was recorded. GDC buffer layer was used between YSZ electrolyte and LSCF cathode to prevent chemical reaction in the YSZ electrolyte and LSCF cathode interface. The electrochemical performance of cells with the SFM and the Ni–YSZ anodes in the same configuration was measured for comparison. As depicted in Fig. 6(c), the OCV of the cell fuelled with H_2 was 1.07 V at 800 °C, close to the value calculated from the Nernst equation. The single cells with the SLFM2 anode

achieved improved maximum power density (MPD = 885 mW cm^{-2}) in slightly humidified H_2 at 800 °C compared to that of the cells with the SFM (740 mW cm^{-2}) and the Ni–YSZ anode (553 mW cm^{-2}) in the same configuration. Additionally, when operating in wet CH_4, the SLFM2–based cell exhibited attractive electrochemical performance with a MPD of 790 mW cm^{-2} at 800 °C, which is much higher than that of the SFM–based cell (659 mW cm^{-2}), as shown in Fig. 6(d). The enhanced electrocatalytic activity of SLFM2 toward CH_4 oxidation could be associated with the improved electrode reaction kinetics. The SLFM2–based cell delivered stable voltage during the short-term stability test with no obvious carbon fibers or carbon particles observed by the post-exposure characterization of the spent cell. This suggests an excellent electrocatalytic activity of SLFM2 toward methane oxidation and good tolerance to carbon deposition in methane (see Supplementary Fig. S8 and S9).

The catalytic activity for methane selective oxidation over the SLFM catalysts was further investigated, as presented in Fig. 6(e). In all cases, H_2 and CO were the primary products although some CO_2 was detected at the initial stage of reaction during catalytic oxidation of methane. The catalytic activity was estimated by the temperature at which 90% conversion (T_{90}) was attained. The kinetic curve of SFM with a T_{90} of 825 °C was similar to the catalytic kinetics of SFM for methane combustion reported by Falcón et al.[36] The catalytic activity of the SLFM2 catalyst with a T_{90} of 775 °C was obviously better than that of the undoped SFM catalyst. However, excess La in SLFM ($0.6 \le x \le 1$) shifted the T_{90} to a higher value (900 °C ≤ T_{90} ≤ 1000 °C). Therefore, the sufficient methane oxidation was likely to be responsible for the high power-output of cell with the SLFM2 anode operated in slightly humidified CH_4.

Fig. 6(f) shows the methane conversion, product selectivity and $n(H_2)/n(CO)$ with time-on-stream over the SLFM2 catalyst at 800 °C. At the initial stage (region I), approximately 90% of CH_4 conversion with high syngas (H_2 and CO) selectivity indicates that the partial oxidation of methane with the lattice oxygen on the catalyst surface occurred immediately. Meanwhile, a CO_2 selectivity of > 4% was observed, suggesting the total oxidation of methane with the adsorbed oxygen on the catalyst surface.[30] CH_4 conversion stabilized at > 99% (region II) after 3 min with a desired H_2/CO molar ratio close to 2.0, indicating the fast and sufficient reaction without obvious CH_4 cracking. The CO_2 selectivity decreased to close to zero because of the fast depletion of the adsorbed oxygen, whereas the syngas selectivity reached a steady state because the bulk oxygen favorably evolved into surface oxygen to contribute to the partial oxidation of methane. The good catalytic stability suggests the matching between the mobility of lattice oxygen and the dissociation rate of methane that requires fast oxygen mobility in the catalyst. In the region III, a H_2/CO ratio close to 3 was observed with an increased H_2 selectivity but decreased CO selectivity. This might be because of the consumption of lattice oxygen and the deep reduction of the catalyst, which would induce the appearance of methane cracking.

In a real SOFC operating condition, the electrolyte delivers the oxygen ions from the cathode to the anode side to supply the lattice oxygen of the anode, contributing to the fuel oxidation. Methane oxidation is supposed to occur on the surface of the anode, which acts as an oxygen carrier. La substitution for Sr combined with the reduction of Fe/Mo cations at the initial state, generate plenty of oxygen vacancies that would favor the lattice-oxygen transfer from bulk to the surface. Meanwhile, the resupply of oxygen from the electrolyte would balance the oxygen consumption, thus leading to

Table 2 DFT-GGA+U ($(U–J)_{Fe}$ = 4.0 eV) AD formation energy of $Sr_{1.8}La_{0.2}FeMoO_{6-\delta}$ containing a pair of Fe_{Mo}–Mo_{Fe} antisite defect[a]; Oxygen-vacancy formation energy of $Sr_{1.8}La_{0.2}FeMoO_{6-\delta}$ with and without ADs.

$E_{form}O^*$(eV)	$Sr_7LaFe_4Mo_4O_{23}$		
O^*_{ab}	4.11		
O^*_c	3.69		
$E_{form}AD$(eV)	AD:$Sr_7LaFe_4Mo_4O_{24}$		
	Mo–Fe_{diag}	Mo–Fe_{ab}	Mo–Fe_c
	0.28	0.30	0.61
$E_{form}O^*$(eV)	AD:$Sr_7LaFe_4Mo_4O_{23}$		
	Mo–Fe_{diag}	Mo–Fe_{ab}	Mo–Fe_c
Fe_{Mo}–O^*_{ab}–Fe	2.64	2.52	3.05
Fe_{Mo}–O^*_c–Fe	2.79	3.09	–
Mo_{Fe}–O^*_{ab}–Mo	3.74	3.95	–
Mo_{Fe}–O^*_c–Mo	3.64	3.96	3.90

[a]Mo and Mo_{Fe} are aligned antiferromagnetically and ferromagnetically to the Fe atoms on the right site, respectively.

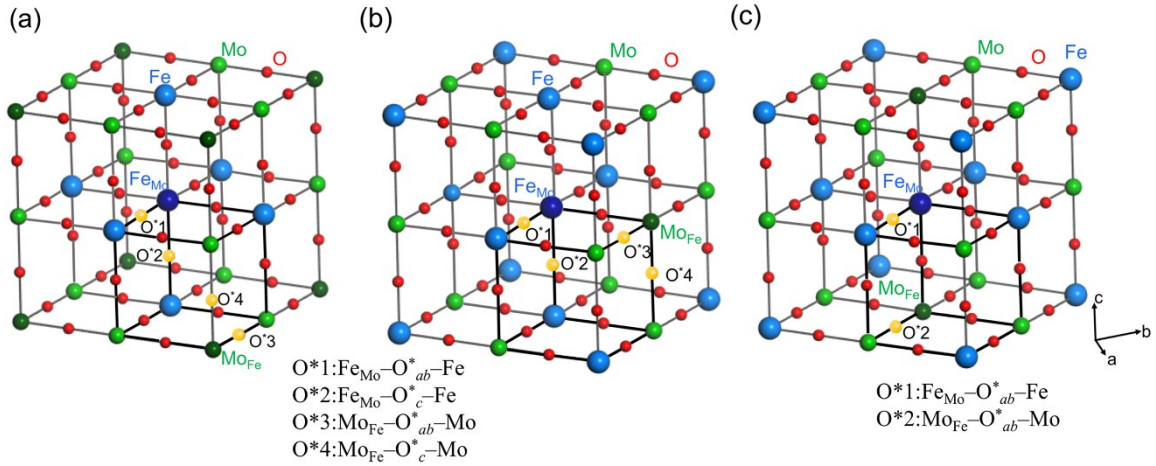

Fig. 7 (a) Oxygen vacancies in $Sr_7LaFe_4Mo_4O_{24}$ ($4Sr_{1.8}La_{0.2}FeMoO_{6-\delta}$) with anti-site defects: (a) along the diagonal, (b) in the *ab* plane, and (c) along the *c* axis of the cube.

a stable power output under methane. In order to better understand the oxygen transportation kinetics that leads to the excellent electrocatalytic activity of the SLFM2 anode toward fuel oxidation, first principles computations were performed to investigate the effect of La doping on the formation of the ADs and oxygen vacancies. Since the oxygen-migration barrier was not affected significantly with La doping, we only present the formation energies of oxygen vacancy and ADs.

Oxygen-vacancy formation energy ($E_{form}O^*$) of the AD-free $Sr_7LaFe_4Mo_4O_{24}$ was first modeled by removing one neutral O atom from the supercell (Supplementary Fig. S10). Exchanging one pair of Fe_{Mo}–Mo_{Fe} lies within the range of our experimental AD degrees: between 84.31 and 34.92. Three different Fe_{Mo}–Mo_{Fe} arrangements in the stoichiometric structures have been considered, including the Fe_{Mo}–Mo_{Fe} exchanges along the diagonal, in the *ab* plane, and along the *c* axis of the cube, as presented in Supplementary Fig. S11. Table 2 summarizes the $E_{form}O^*$ and AD formation energy ($E_{form}AD$) of SLFM2 for different cases.

The calculated $E_{form}O^*$ of the AD-free $Sr_7LaFe_4Mo_4O_{24}$ was 3.69 and 4.11 eV along the *c* axis and in the *ab* plane, which is close to that of the un-doped AD-free $Sr_7Fe_4Mo_4O_{24}$ reported (3.94 and 4.01 eV). [15] As expected, the calculated $E_{form}AD$ of $Sr_7LaFe_4Mo_4O_{24}$ is 0.28, 0.30, and 0.61 eV with an AD along each direction, much smaller than the $E_{form}O^*$ of the AD-free supercell. This indicates that Fe_{Mo}–Mo_{Fe} exchanges are much easier to achieve than O^* in the SLFM2, especially along the supercell diagonal. In addition, the minimum $E_{form}AD$ of slightly La-doped $Sr_2FeMoO_{6-\delta}$ is also smaller than the un-doped counterpart reported (0.42 eV).[37] Thus, the ADs are more readily to form in SLFM2 compared with SFM, consistent with the increase in AD concentration with La doping. Upon AD formation, Fig. 7 shows all O^* positions considered (δ = 0.25). The results reveal that $E_{form}O^*$ (Fe_{Mo}–O–Fe) shows lower value than that of $E_{form}O^*$ (Mo_{Fe}–O–Mo), which are consistent with the trend reported for similar structures.[25,37] This is because the breaking of Fe–O bond is easier than that of the Mo–O bond. [15] The results also lead to a satisfactory agreement with our experimental observations. With La doping in SFM, the $E_{form}O^*$ has been significantly reduced, accompanied with a drastic increase in AD concentration. Consequently, small La incorporation into SFM facilitates the formation of ADs and oxygen-vacancies, where the AD formation promotes the oxygen-vacancy formation simultaneously, accounting for the excellent electrochemical activity of the SLFM2 anode.

5. Conclusions

$Sr_{2-x}La_xFeMoO_{6-\delta}$ ($0 \leq x \leq 1$) double perovskites have been designed by electron doping to demonstrate their performance as anode materials for SOFCs. A-site La doping of SFM can introduce phase transition, alter conducting behavior and consequently affect its electrocatalytic activity for fuel oxidation. The SLFM2 has been shown to have the optimized La amount with the highest electrical conductivity and electrochemical performance in the SLFM series because of the desired oxygen vacancy concentration. XRD refinement suggests the increase in Fe/Mo disorder with La doping. First principles calculations reveal that the anti-site defect is the main reason behind the improvement in its anodic performance. Most excess electrons introduced by La^{3+} for Sr^{2+} are injected into the Mo t_{2g} orbital, resulting in increased AD concentration because of the decreased difference of valences between Fe and Mo. YSZ electrolyte-supported SOFCs with the SLFM2-anode have enhanced electrochemical performance than that with the SFM anode in H_2 at 800 °C. SOFCs with SLFM2-anode have demonstrated excellent and stable performance under direct CH_4 operation. This is attributed to the high catalytic activity for methane selective oxidation of the SLFM2 catalyst with a methane conversion of > 99% at 800 °C. The identification of oxygen-vacancy formation energy, AD formation energy and oxygen transportation kinetics reveals the mechanism for fuel oxidation and provides a new pathway to improve the electrochemical activity of catalysts with the participation of oxygen in energy conversion and storage devices.

Conflicts of interest

There are no conflicts to declare.

Acknowledgements

This work was primarily supported by National Key R&D Program of China (2017YFA0700104), the US National Science Foundation (DMR–1832809), the National Natural Science Foundation of China (91745203, 51102079), and the Program for Science & Technology Innovation Talents in Universities of Henan Province (15HASTIT047). X. Y. thanks the financial support from the State-Sponsored Scholarship for Graduate Students from China Scholarship Council.

References

1 J. Hwang, R. R. Rao, L. Giordano and Y. Katayama, Y. Yu, S. H. Yang, *Science,* 2017, **358**, 751.
2 C. Sun and U. Stimming, *J. Power Sources,* 2007, **171**, 247.
3 J. W. Fergus, *Solid State Ionics,* 2006, **177**, 1529.
4 J. H. Koh, Y. S. Yoo, J. W. Park and H. C. Lim, *Solid State Ionics,* 2002, **149**, 157.
5 Z. Xie, H. Zhao, Z. Du, T. Chen, N. Chen, X. Liu and S. J. Skinner, *J. Phys. Chem. C,* 2012, **116**, 9734.
6 J. Sunarso, S. S. Hashim, N. Zhu and W. Zhou, Prog. *Enrgy Combust. Sci.,* 2017, **61**, 57.
7 X. Yang, J. Liu, F. Chen, Y. Du and A. Deibel, T. He, *Electrochim. Acta,* 2018, **290**, 440.
8 Q. Liu, C. Yang, X. Dong and F. Chen, *Int. J. Hydrogen Energy,* 2010, **35**, 10039
9 J. Rager, M. Zipperle, A. Sharma and J. MacManus-Driscoll, *J. Am. Ceram. Soc.,* 2004, **87**, 1330
10 L. Zhang, Q. Zhou, Q. He and T. He, *J. Power Sources,* 2010, **195**, 6356.
11 Z. Du, H. Zhao, S. Yi, Q. Xia, Y. Gong, Y. Zhang, X. Cheng, Y. Li, L. Gu and K. Swierczek, *ACS Nano,* 2016, **10**, 8660.
12 Y. Huan, Y. Li, B. Yin, D. Ding and T. Wei, *J. Power Sources,* 2017, **359**, 384.
13 I. Hussain, M. S. Anwar, J. W. Kim, K. C. Chung and B. H. Koo, *Ceram. Int.,* 2016, **42**, 13098.
14 T. O. Y. Tomioka, Y. Okimoto, R. Kumai, and K. I. Kobayashi, *Phys. Rev. B,* 2000, **61**, 422.
15 A. B. Muñoz-García and M. Pavone, E. A. Carter, *Chem. Mater.,* 2011, **23**, 4525.
16 [16] D. Stoeffler, *J. Phys.: Condens. Matter,* 2012, **24**, 046004.

17 Y. C. Hu, J. J. Ge, Q. Ji, Z. S. Jiang, X. S. Wu and G. F. Cheng, *Mater. Chem. Phys.,* 2010, **124**, 274.
18 X. Yang, D. Panthi, N. Hedayat, T. M. He and Y. H. Du, *Electrochem. Commun.,* 2018, **86**, 126.
19 D. D. Sarma, P. Mahadevan, T. Saha-Dasgupta and S. Ray, A. Kumar, *Phys. Rev.Lett.,* 2000, **85**, 2549.
20 F. Azizi, A. Kahoul and A. Azizi, *J. Alloys Compd.,* 2009, **484**, 555.
21 J. Navarro, C. Frontera, L. Balcells and B. Martinez, J. Fontcuberta, *Phys. Rev. B,* 2001, **64**, 092411.
22 A. Kahoul, A. Azizi, S. Colis, D. Stoeffler, R. Moubah, G. Schmerber, C. Leuvrey and A. Dinia, *J. Appl. Phys.,* 2008, **104**, 123903.
23 M. Cernea, F. Vasiliu, C. Bartha, C. Plapcianu and I. Mercioniu, *Ceram. Int.,* 2014, **40**, 11601.
24 S. Sengodan, S. Choi, A. Jun, T. H. Shin, Y. W. Ju, H. Y. Jeong, J. Shin, J. T. Irvine and G. Kim, *Nat. mater.,* 2015, **14**, 205.
25 Z. Du, H. Zhao, S. Li, Y. Zhang, X. Chang, Q. Xia, N. Chen, L. Gu, K. Świerczek, Y. Li, T. Yang and K. An, *Adv. Energy Mater.,* 2018, **8**, 1800062.
26 P. Kumar, N. K. Singh, A. Sinha and P. Singh, *Appl. Phys. A,* 2016, **122**, 828.
27 D. Sánchez, J. A. Alonso, M. García-Hernández, M. J. Martínez-Lope, J. L. Martínez and A. Mellergård, *Phys.Rev.B,* 2002, **65**, 263.
28 M. T. Anderson, K. B. Greenwood, G. A. Taylor and K. R. Poeppelmeier, *Prog. Solid State Chem.,* 1993, **22**, 197.
29 R. S. Hu, Y. Q. Bai, H. Y. Du, H. M. Zhang, Y. F. Du, J. Zhang and Q. H. Zhou, *J. Rare Earths,* 2015, **33**, 1284.
30 K. Zhao, L. Li, A. Zheng, Z. Huang, F. He, Y. Shen, G. Wei, H. Li and Z. Zhao, *Appl. Energy,* 2017, **197**, 393.
31 P. Xiao, L. Zhong, J. Zhu, J. Hong, J. Li, H. Li and Y. Zhu, *Catal. Today,* 2015, **258**, 660.
32 Y. H. Huang, G. Liang, M. Croft, M. Lehtimaki, M. Karppinen and J. B. Goodenough, *Chem. Mater.,* 2009, **21**, 2319.
33 R. I. Dass. Y. H. Huang, Z. L. Xing and J. B. Goodenough, *Science,* 2006, **312**, 254.
34 Y. Ji, Y. H. Huang, J. R. Ying and J. B. Goodenough, *Electrochem. Commun.,* 2007, **9**, 1881.
35 S. R. G. Narsinga Rao, C. Y. Mou and J. W. Chen, *J. Magn. Magn. Mater*., 2006, **229**, 348.
36 J. A. B. H. Falcón, G. Araujo, M. T. Casais, M. J. Marťınez-Lope, J. A. Alonso and J. L. G. Fierro, *Appl. Catal., B,* 2004, **53**, 37.
37 J. Navarro, J. Nogués, J. S. Muñoz and J. Fontcuberta, *Phys. Rev. B,* 2003, **67**, 174416.